Iterative sensitivity matrix-based magnetic resonance conductivity tensor imaging

Evren DEĞİRMENCİ[*]

Department of Electrical-Electronics Engineering, Faculty of Engineering, Mersin University, Mersin, Turkey

Abstract: Magnetic resonance conductivity tensor imaging (MRCTI) reconstructs high-resolution anisotropic conductivity images, which are proved to have critical importance in radio-oncological imaging as well as source localization fields. In the MRCTI technique, linearly independent current injections are applied to the region to be imaged and resulting magnetic flux densities are measured using magnetic resonance imaging techniques. In this study, a novel iterative reconstruction algorithm based on a sensitivity matrix approach is proposed and tested using both simulated and experimental measurements. Obtained results show that the proposed technique can reconstruct anisotropic conductivity images with high and position-independent spatial resolution in addition to decreased number of current injection strategies.

Key words: Magnetic resonance imaging, conductivity tensor, anisotropy, reconstruction

1. Introduction

Electrical conductivity distribution is a clinically important information especially in accurate analysis of biosignals such as EEG or ECG and localization of bioelectromagnetic sources, as well as accurate planning of electromagnetic therapeutic techniques [1, 2]. It is also shown that variations among electrical impedances of tissues can be a good marker of pathological changes in human subjects [3]. For example, some studies in the literature report that the electrical impedance of malignant tumors is significantly lower than that of benign lesions and normal tissues [4–6].

The electrical impedance tomography (EIT) technique was first proposed to measure electrical conductivity in the human body noninvasively [7]. As the results of studies conducted for more than 30 years, EIT evolved into a technique having clinical applications [8]. However, since the technique has low reconstruction sensitivity for regions far from measurement points, it cannot be ranked among high-resolution conductivity imaging techniques. Magnetic resonance electrical impedance tomography (MREIT) was then proposed to image electrical conductivity with high and position-independent resolution [9]. MREIT is today on the way to becoming a clinically applicable technique [10–12]. In this technique, injected or induced currents are applied to the region of interest as in EIT, but in this case, magnetic flux densities generated by these currents are measured within the body using magnetic resonance imaging (MRI) techniques with equal sensitivity. Then conductivity distribution is calculated utilizing either the z-component of magnetic flux density measurement directly (B-based MREIT algorithms) [13–15] or current density distributions obtained from magnetic flux densities using the Biot–Savart law (J-based MREIT algorithms) [16, 17]. Only parallel components of magnetic

---

[*]Correspondence: evrendegirmenci@mersin.edu.tr

flux density with the main magnetic field direction of the MRI system can be measured using MRI techniques. Since Biot–Savart formulation requires three components of magnetic flux density for current density calculation, the body to be imaged should be rotated three times and aligned to the main magnetic field inside the MRI system [18]. Another and more important fact about this technique is that conductivity is assumed to be isotropic in MREIT to simplify the underlying mathematics. However, most of the tissues in the human body have anisotropic conductivity values and therefore the isotropic assumption causes the conductivity images to be erroneous [19].

Magnetic resonance conductivity tensor imaging (MRCTI) was proposed to overcome this problem and to reconstruct high-resolution anisotropic conductivity images [20–22]. As in the MREIT technique, MRCTI uses either magnetic flux density measurements directly (B-based MRCTI algorithms) or current density images obtained using the Biot–Savart law (J-based MRCTI algorithms). Most of the MRCTI reconstruction algorithms proposed to date from both types are examined and compared in terms of reconstruction performances using both simulated and experimental measurements, such as in [22–24]. However, by considering the necessity of body rotation in the MRI system for J-based MRCTI algorithms, it is concluded that the anisotropic Bz sensitivity (ABzS) algorithm is one step ahead among existing algorithms for MRCTI. Today, the major obstacle to clinical application of MRCTI is the number of current injection strategies and the amplitude of the applied current required to achieve an acceptable signal-to-noise ratio (SNR) and therefore high and position-independent reconstruction accuracy. In this study, an iterative sensitivity matrix-based MRCTI algorithm, namely the anisotropic iterative Bz sensitivity (AIBzS) algorithm, is proposed. The aim of the current study is to reach a novel MRCTI reconstruction algorithm with increased accuracy together with decreased number of current drives and therefore to make high-resolution conductivity imaging possible together with less independent current injections.

2. Methods

2.1. Iterative sensitivity matrix-based magnetic resonance conductivity tensor imaging (AIBzS) algorithm

The proposed algorithm is based on the generation of a sensitivity matrix, which relates the perturbation of magnetic flux density for a perturbation in conductivity tensor and repeats this calculation iteratively for more accurate image reconstruction. Sensitivity matrix generation requires the calculation of magnetic flux density for a given tensor distribution. In 2-dimensional MRCTI, the conductivity tensor is defined as a positive definite symmetric matrix $\bar{\bar{\sigma}}(x,y) = \begin{bmatrix} \sigma_{xx} & \sigma_{xy} \\ \sigma_{yx} & \sigma_{yy} \end{bmatrix}$, where σ_{xx} and σ_{yy} are the x and y directed conductivities at (x,y), respectively, and $\sigma_{xy} = \sigma_{yx}$. Poisson's equation relates the conductivity tensor and potential field nonlinearly as

$$\bigtriangledown \cdot (\bar{\bar{\sigma}}(x,y) \bigtriangledown \varphi(x,y)) = 0, \quad (x,y)\epsilon D, \tag{1}$$

where φ is the potential field at (x,y) in the imaging slice D and '$\bigtriangledown\cdot$' stands for divergence. This equation is solved as a boundary value problem together with the following Neumann boundary conditions:

$$-\bar{\bar{\sigma}}(x,y)\frac{\partial\varphi(x,y)}{\partial n} = \begin{cases} J, & \text{on positive current electrode,} \\ -J, & \text{on negative current electrode,} \\ 0, & \text{otherwise,} \end{cases} \tag{2}$$

and the potential field is obtained in D. Here, n is the unit normal at the boundary and J is the current density. In this study, the finite element method (FEM) is used to solve the equation set of Eqs. (1) and (2) in D. Then the solution is extracted to an n-by-m matrix for further processing. After obtaining potential field distribution, electric field and current density distributions are calculated in D as

$$\vec{E}(x,y) = -\bigtriangledown \varphi(x,y), \tag{3}$$

$$\vec{J}(x,y) = \bar{\bar{\sigma}}(x,y)\vec{E}(x,y). \tag{4}$$

Finally, the magnetic flux density distribution generated by this current density distribution is calculated using the following Biot–Savart relation:

$$B(x,y) = \frac{\mu_0}{4\pi} \int \frac{\vec{J}(x,y)dD \times \hat{a}_R}{R^2}. \tag{5}$$

Here, μ_0 is the free space permeability, $\hat{a}_R$ is the unit vector from the source point (x', y') to the field point (x, y), and R is the distance between source and field points.

The processes from Eq. (1) to Eq. (5) constitute the forward problem of MRCTI and enable one to calculate magnetic flux density for a known tensor and current density distribution. On the other hand, the inverse problem of MRCTI involves reconstruction of tensor distribution for measured magnetic flux density. Details on obtaining magnetic flux density generated by an applied current from MR phase images can be found in [24]. Since the component of magnetic flux density in the direction of the main magnetic field, which is thought of as the z-component, can be measured using MR and since the measurement of other components requires body rotation in the MR system, the reconstruction of the tensor distribution process in the current study is built up using only the z-component of magnetic flux density. The main idea of the MRCTI reconstruction algorithm proposed in this study is to generate a sensitivity matrix that relates the change in tensor distribution to the change in the z-component of magnetic flux density and to update this sensitivity matrix iteratively for updated anisotropic conductivity distribution. Details of the algorithm are explained step by step below:

1. First, an n-by-m uniform tensor distribution, $\bar{\bar{\sigma}}(x,y) = \begin{bmatrix} 1 & 0 \\ 0 & 1 \end{bmatrix}$, $\forall (x,y)\epsilon D$, is assumed and corresponding magnetic flux density is calculated using Eqs. (1) to (5) using the FEM for each current injection profile. In this study, two independent current injection profiles were used. n and m values are determined by the size of measured MR images.

2. For sensitivity matrix calculation, each element of $\bar{\bar{\sigma}}(x,y)$ in D is changed by adding a predefined perturbation value and corresponding magnetic flux density is recalculated. More clearly, the perturbation value is first added to each element (pixel) of σ_{xx} separately and corresponding magnetic flux density is obtained in D for each pixel-wise conductivity perturbation. Perturbation value is selected as 0.01 S/m, which corresponds to the 1% of initial conductivity value for both directions. For the next iterations, it is selected as the 1% of absolute mean of reconstructed conductivity tensor components. Increasing this value can increase the convergence speed of the algorithm but the reconstruction error would be high. On the other hand, decreasing the value of perturbation will decrease the convergence speed while reaching low reconstruction error values. Then the magnetic flux density distribution obtained

for uniform conductivity distribution is subtracted from each of the magnetic flux density distributions calculated for pixel-wise conductivity perturbations and the difference in magnetic flux density generated by pixel-wise conductivity perturbation is obtained. These calculations give n-by-m magnetic flux density perturbations corresponding to the perturbation of each element in σ_{xx}. Then the obtained magnetic flux density perturbation matrices are divided into the conductivity perturbation value to achieve a magnetic flux density perturbation for a unit change in conductivity. This calculation is repeated for each pixel element of σ_{xx} and then the results are converted to an $n \times m - by - 1$ column form and laid together to form an $n \times m - by - n \times m$ sensitivity matrix for all pixel-wise perturbations in σ_{xx}. The same calculations are repeated for perturbations in σ_{yy} and $\sigma_{xy} = \sigma_{yx}$ and a complete sensitivity matrix with $(n \times m) - by - (3 \times n \times m)$ elements is constituted.

3. Steps 1 and 2 are repeated for every current injection drive. The obtained sensitivity matrices are merged vertically and the main sensitivity matrix **S**, which relates the magnetic flux density perturbation to the pixel-wise perturbation of each element of the conductivity tensor for all current drives, is obtained.

4. For the reconstruction of the conductivity tensor, the calculated sensitivity matrix is used to linearize magnetic flux density change around conductivity change as

$$\triangle \mathbf{b} = \mathbf{S} \triangle \bar{\bar{\sigma}} = \mathbf{S} \begin{bmatrix} \triangle \sigma_{xx} \\ \triangle \sigma_{xy} \\ \triangle \sigma_{yy} \end{bmatrix}, \tag{6}$$

where $\triangle \mathbf{b}$ is the difference between the measured z-component of magnetic flux density and the one calculated for uniform tensor distribution, **S** is the sensitivity matrix, and $\triangle \bar{\bar{\sigma}}$ is the variation of the conductivity tensor from uniform distribution. For the solution of $\triangle \bar{\bar{\sigma}}$, the inverse of the sensitivity matrix is required, but the inverse of the matrix cannot be taken directly since **S** is not square and is ill-posed in general. The truncated singular value decomposition (TSVD) method could be used for the inversion of the matrix, but since the TSVD method requires the user to select the truncation level, it will be an obstructive method in an iterative algorithm. In this study the Tikhonov regularization method is used. Including the regularization parameter, λ, Eq. (6) becomes

$$\mathbf{S}^T \triangle \mathbf{b} = (\mathbf{S}^T \mathbf{S} + \lambda \mathbf{I}) \triangle \bar{\bar{\sigma}}. \tag{7}$$

Here, **I** is the identity matrix and $\mathbf{S}^T$ stands for the transpose of **S**. Optimal regularization parameter λ is selected using l-curve optimization, in which the solution and residual norms of the equation for different λ values are calculated and the optimal λ is selected at which regularization error and perturbation error are minimum. Then, using this regularization parameter, Tikhonov regularization is performed and $\bar{\bar{\sigma}}$ is calculated. $\bar{\bar{\sigma}}$ involves the deviation values of tensor components from initial distribution for every pixel. Therefore, by adding $\bar{\bar{\sigma}}$ to the initial tensor distribution, first the anisotropic conductivity distribution of the algorithm is obtained. Since the regularization parameter is searched for the minimization of mean difference between the z-components of measured and calculated magnetic flux density, fast convergence and progression to the global minima are ensured.

5. At this step, mean absolute difference, given in Eq. (8), is calculated for x and y components of the

conductivity tensor for two consecutive iterations.

$$\epsilon = \frac{1}{N} \sum_{j=1}^{N} |\sigma_{j_u}^{i} - \sigma_{j_u}^{i-1}|$$

(8)

Here, u is the tensor component index (xx or yy), σ_j^i and σ_j^{i-1} are the reconstructed conductivity values of the jth element reached at the end of current and previous iterations, respectively, and N is the total number of pixels in the images. If ϵ is lower than 0.02 for both conductivity components, then the iterations are terminated; otherwise, a new conductivity distribution is used as initial tensor distribution and steps 1 to 4 are repeated using this new distribution.

It is important to note that only relative conductivity values (contrast images) can be reconstructed using magnetic flux density measurements, since all tensor distributions satisfying the same relative distribution will produce the same magnetic flux density distribution. Therefore, a scale factor is required to find the exact tensor distribution. In this study one bipolar voltage measurement is used to calculate the true conductivity distribution.

2.2. Test phantoms for performance evaluation

In order to test the proposed algorithm, three simulation measurements and one experimental magnetic flux density measurement are employed.

For simulation measurements, a 2-dimensional square model with edge length of 9 cm is constructed in a computer environment. Four 1-cm electrodes are placed on the middle of all edges for current injection. A 20-mA current is injected in vertical and horizontal trajectories using E1-E2 and E3-E4 electrode pairs, respectively. Geometry and electrode placement of simulation models are shown in Figure 1. Potential measurements are simulated on current injecting electrodes for each current injection profile.
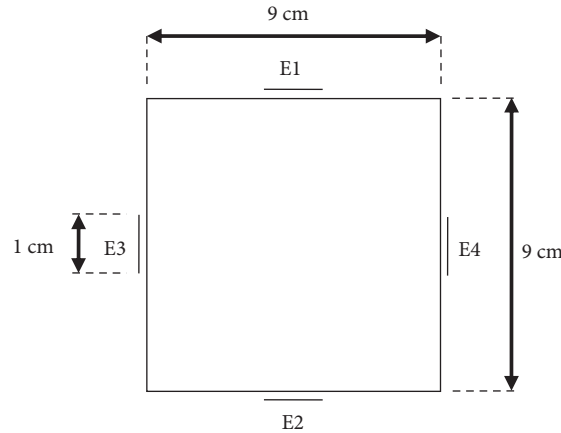
Figure 1. Dimensions and electrode placement of simulation models.

Conductivity tensor distribution of the first simulation phantom is designed to evaluate the reconstruction accuracy performance of the proposed algorithm. For this purpose, a circle-shaped object having a radius of 15.75 mm with conductivity value of 0.4 S/m is modeled in the x-direction (σ_{xx}), while a square-shaped object having edge length of 31.25 mm with conductivity value of 0.6 S/m is modeled in the y-direction (σ_{yy}). The

background conductivity is modeled as 0.2 S/m in both directions to simulate average tissue conductivity for the human body [25]. Conductivity distributions of tensor components of the first computer model are shown in Figures 2a and 2b.

(a)   (b)
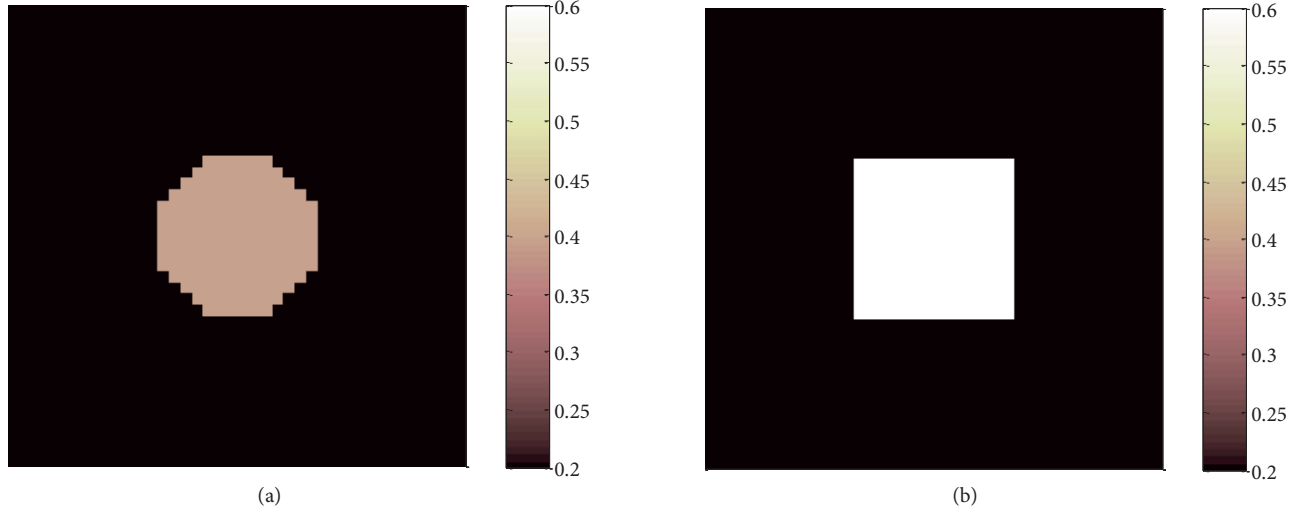
Figure 2. Conductivity images of the first computer model: (a) x-directed conductivity (σ_{xx}^{object}=0.4 S/m, $\sigma_{xx}^{background}$=0.2 S/m), (b) y-directed conductivity (σ_{yy}^{object}=0.6 S/m, $\sigma_{yy}^{background}$=0.2 S/m). $\sigma_{xy} = \sigma_{yx} = 0$ for all regions in the model.

It is important to note that the tensor distribution of the first computer model is modeled similarly to the one used in [22] in order to compare the reconstruction performance of the proposed algorithm with other MRCTI algorithms in a controlled manner. The second computer model is designed to evaluate spatial resolution properties of the proposed algorithm throughout the field of view (FOV). A total of 25, one-pixel-sized (2.25 mm in this study) anisotropic conductivity perturbations are distributed throughout the FOV to reveal the space dependency of the tensor reconstruction using the proposed algorithm. The x- and y-directed conductivities of one-pixel-sized perturbations are selected as 2 S/m and 0.02 S/m, respectively, while the background conductivity is again 0.2 S/m in both directions. Tensor distribution of the second model is shown in Figures 3a and 3b.

In order to analyze the reconstruction linearity property of the proposed technique, a third computer model is designed as seen in Figures 4a and 4b. In this model, a square object with 2.25-mm side length is placed in the middle of the model having an isotropic background conductivity value of 0.2 S/m. The x-directed conductivity of the object is modeled as 1 S/m and 2 S/m separately, in order to investigate the behavior of the algorithm for high conductivity contrasts (Figure 4a). The y-directed conductivity of the square object is modeled as 0.2 S/m, which is equal to the background (Figure 4b).

Finally, to evaluate the performance of the proposed algorithm under experimental conditions, magnetic flux density measurements obtained from the 0.15-T METU MRI system are utilized. The experimental phantom used in the study is a square slice of 9 cm by 9 cm with 1-cm thickness, which is also used in [23]. A 3-D drawing of the experimental phantom is presented in Figure 5. Four 1 cm by 1 cm recessed electrodes are used for current injection. Only opposite electrode pairs are used to inject the 20-mA current generated by the voltage-controlled constant current source; therefore, the z-component of magnetic flux density is only measured for vertical and horizontal current trajectories as in the simulation studies. Voltage measurements are also done

(a) (b)
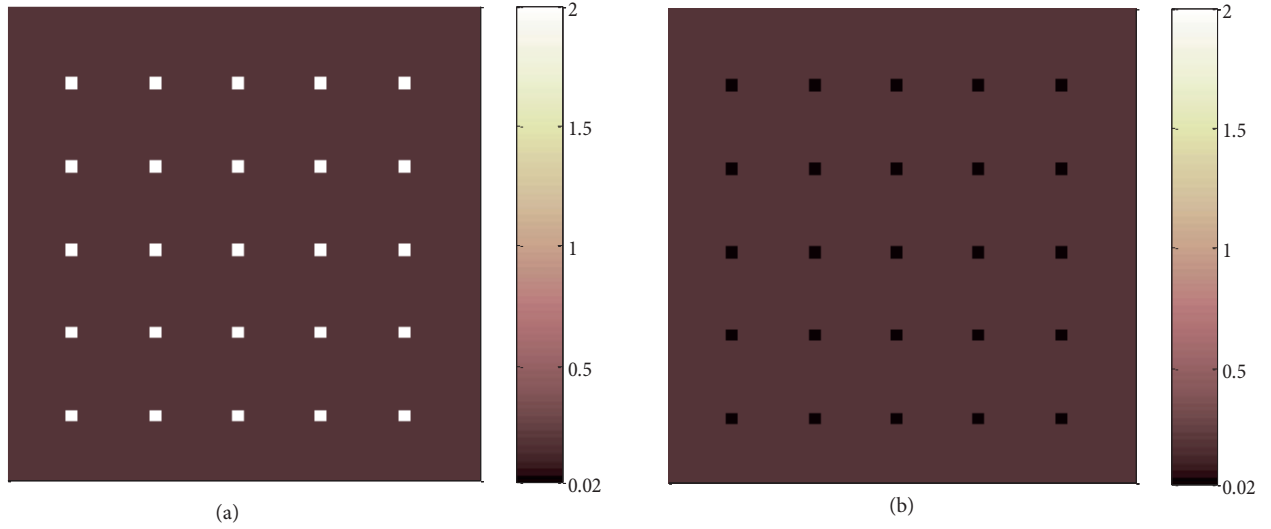
Figure 3. Conductivity images of the second computer model: (a) x-directed conductivity ($\sigma_{xx}^{objects}$=2 S/m, $\sigma_{xx}^{background}$=0.2 S/m), (b) y-directed conductivity ($\sigma_{yy}^{objects}$=0.02 S/m, $\sigma_{yy}^{background}$=0.2 S/m). $\sigma_{xy} = \sigma_{yx} = 0$ for all regions in the model.

(a) (b)
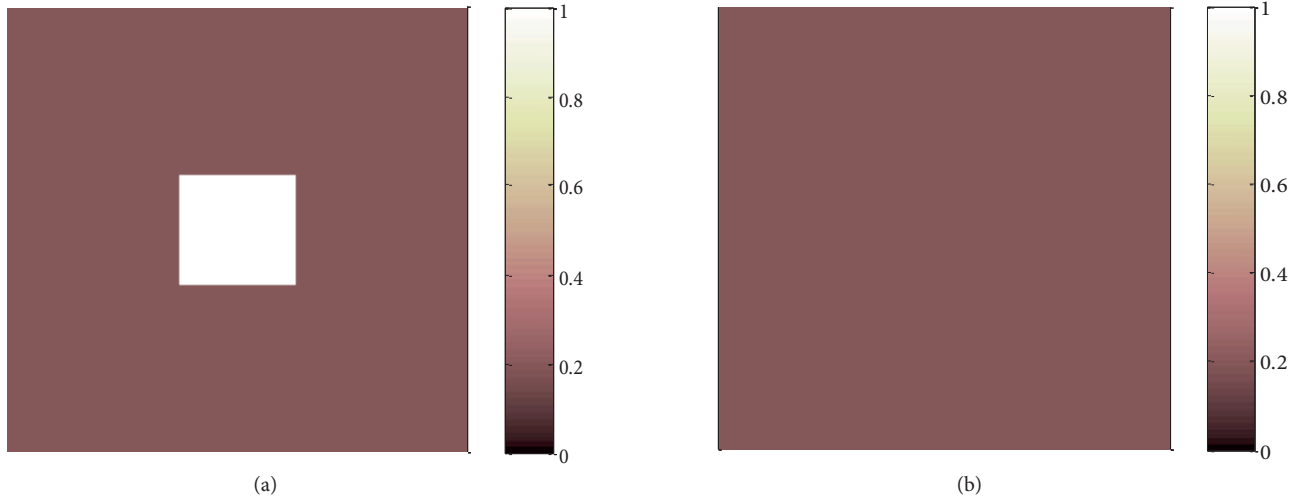
Figure 4. Conductivity images of the third computer model: (a) x-directed conductivity (σ_{xx}^{object}=1 S/m, $\sigma_{xx}^{background}$=0.2 S/m), (b) y-directed conductivity (σ_{yy}^{object}=0.2 S/m, $\sigma_{yy}^{background}$=0.2 S/m). $\sigma_{xy} = \sigma_{yx} = 0$ for all regions in the model.

through current-injecting electrodes using a hand-held digital voltmeter. Seven thin insulator layers having holes on them are placed inside the phantom and the remaining part of the phantom is filled with a saline solution having conductivity of 2 S/m.

3. Results and discussion

All reconstructed anisotropic conductivity images of the proposed algorithm are obtained using two current injection profiles (opposite profiles in this study). Figures 6a–6c show the reconstructed tensor components for computer model 1 after the 30th iteration. In order to quantize the results for comparison, the L2 relative error norm, given in Eq. (9), is utilized:
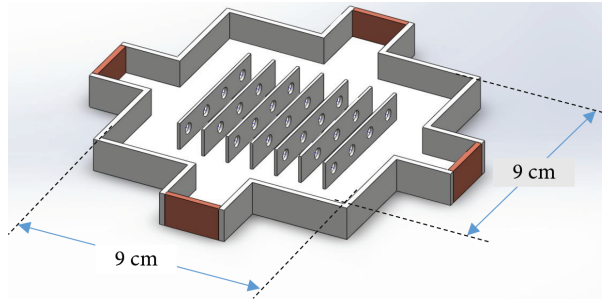
Figure 5. 3-D drawing of experimental phantom used in the study.

$$\epsilon_{\sigma_u} = \sqrt{\frac{1}{N} \sum_{j=1}^{N} \frac{(\sigma_{jt_u} - \sigma_{jr_u})^2}{(\sigma_{jt_u})^2}} \times 100, \tag{9}$$

where u is the tensor component index, which can be xx or yy; σ_{jt} and σ_{jr} are the true and the reconstructed conductivity values in any direction for the jth element; and N denotes the total number of pixels in the image. For off-diagonal components of the conductivity tensor, the mean of the reconstructed image is calculated for quantization. Table 1 gives the calculated error values for the reconstructed images in Figure 6.
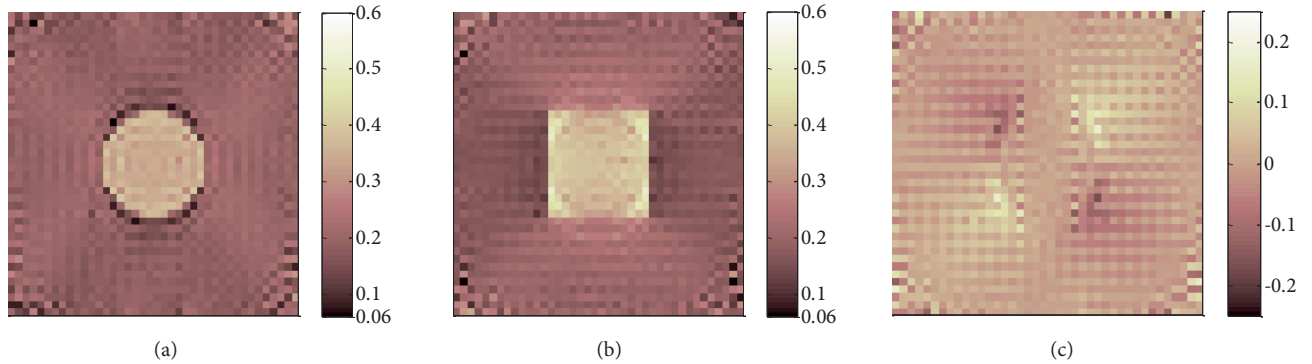
Figure 6. Reconstruction results for the first computer model: (a) σ_{xx}, (b) σ_{yy}, (c) $\sigma_{xy} = \sigma_{yy}$.

Table 1. Reconstruction error for the first computer model.

	$\epsilon_{\sigma_{xx}}(\%)$	$\epsilon_{\sigma_{yy}}(\%)$	$\sigma_{xy} = \sigma_{yx}(Mean)$
Object	13.48	22.07	0.0006
Background	8.35	9.04	0.0010

As seen from the reconstructed tensor images and reconstruction errors, the proposed AIBzS algorithm can reconstruct tensor images with error values of about 20% or less. Unlike the ABzS algorithm proposed in [22], the AIBzS algorithm works in an iterative manner to reduce reconstruction error and, as a result of this, about 10% lower error values with respect to the ABzS algorithm are obtained especially for objects having anisotropic conductivity values. Taking into account that the results in this study are reconstructed using only two magnetic flux density measurements instead of four as in [22], this 10% improvement becomes more remarkable. If two cross current drives are added to the solution set and four current injections are used as in

[22], reconstruction errors decrease to 10.24 and 20.19 for x and y components of the object and 7.17 and 9.87 for corresponding components of the background, respectively, which shows up to 14% increase in reconstruction accuracy using two current injections.

Reconstruction results for the second computer model after the 28th iteration are given in Figures 7a–7c. This computer model is generated with one-pixel-sized point objects distributed over the FOV to investigate spatial and space-dependent resolution properties of the proposed algorithm. In this study, the point spread function (PSF) is used for spatial resolution analysis. Since the true conductivity distribution consists of point objects, the reconstructed distributions of those objects can be regarded as the PSF of the algorithm at corresponding points. Therefore, x- and y-directed profile plots at middle lines of the FOV (red lines in Figures 7a and 7b) are generated and analyzed. These plots are given in Figures 8a–8d, together with true PSF plots (red dashed lines). The results show that the proposed algorithm can reconstruct one-pixel-sized objects again with one pixel size. Since the pixel size is determined by the MR system and is equal to the spatial resolution of MR imaging, it can be said that the proposed algorithm can reconstruct tensor distribution with a spatial resolution equal to MR imaging. When position dependency of the reconstruction is investigated, corners of the FOV are seen to have worse reconstructions. Since the algorithm is based on a sensitivity matrix calculation that relates conductivity change to magnetic flux density change and since the magnetic flux density is directly proportional to the current density, the sensitivity to the regions with low current density will be low. Therefore, low reconstruction accuracy at the corners of the FOV is an expected result since only 2 current injection strategies are employed and they both generate low current density at the corners. Including more magnetic flux density measurements generated by additional current injection strategies will improve the reconstruction performance at the corners. Furthermore, this situation will not arise for circular phantoms or circular bodies such as heads or torsos.
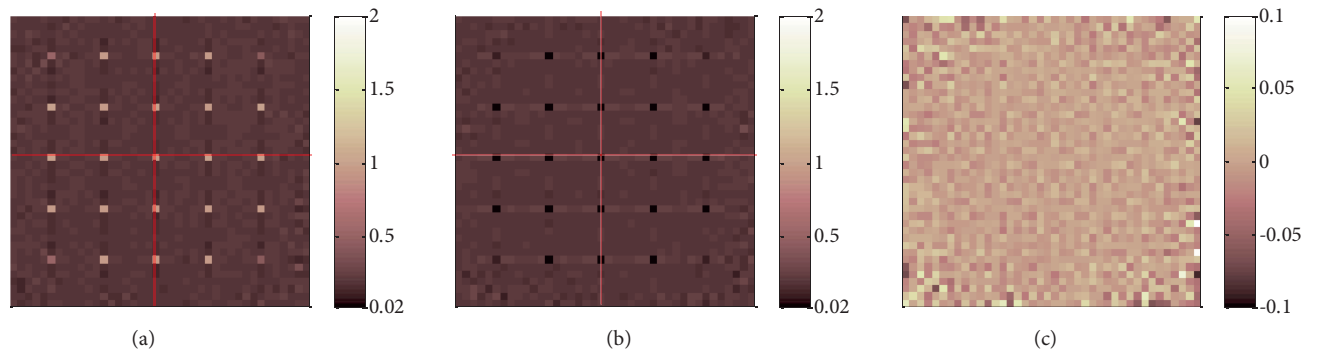
Figure 7. Reconstruction results for the second computer model: (a) σ_{xx}, (b) σ_{yy}, (c) $\sigma_{xy} = \sigma_{yy}$.

Reconstructed tensor components for the third computer model when the x-directed conductivity of the inner object is equal to 1 S/m are shown in Figures 9a–9c. Since the aim of this model is to reveal the linearity property of the proposed algorithm, mean values of reconstructed tensor components for the inner square object are calculated when the true x-directed conductivity is 1 S/m and 2 S/m. The results are given in Table 2.

Values in Table 2 enable us to produce two important conclusions about the proposed algorithm. First, the proposed iterative technique can reconstruct high conductivity contrasts better than other B-based MRCTI techniques when compared with the results in [24]. More clearly, when the true x-directed conductivity of the inner object is 1 S/m and 2 S/m, previously proposed B-based MRCTI algorithms can reconstruct the conductivity values of that object around 0.4 S/m and 0.45 S/m, respectively, but for the proposed algorithm,
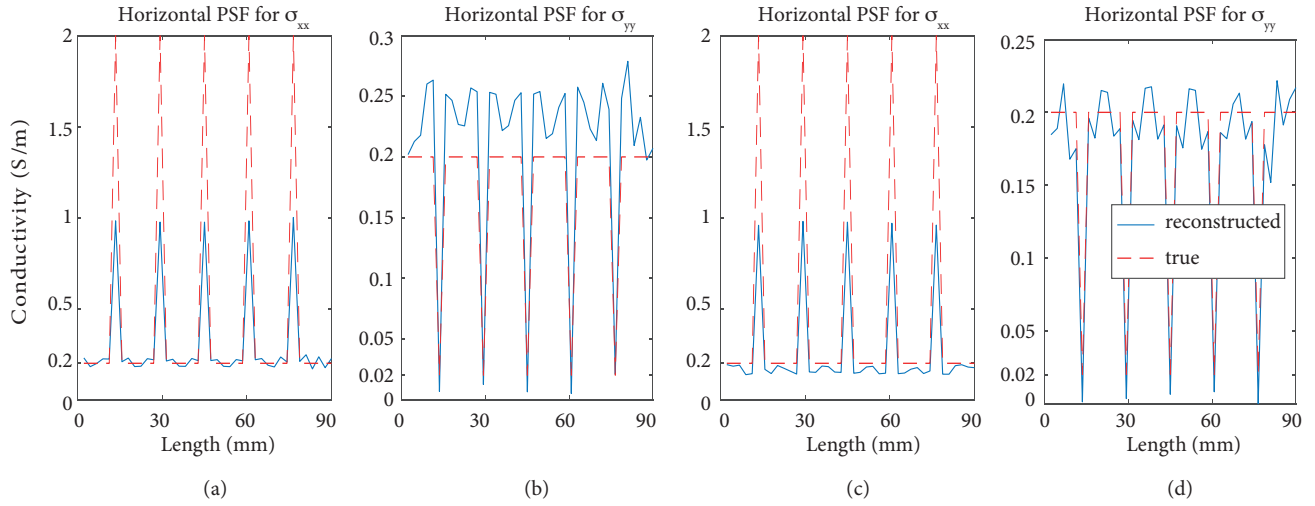
Figure 8. Horizontal and vertical point spread function plots for point objects in σ_{xx} and σ_{yy}.
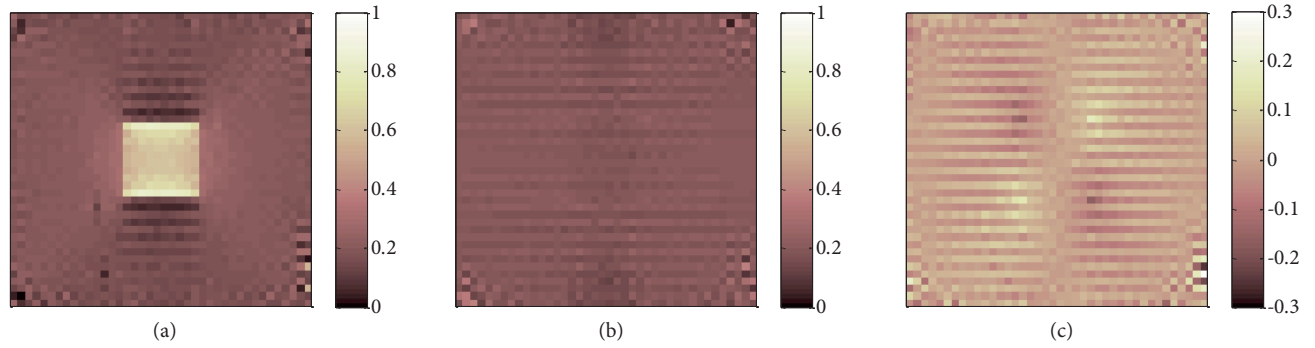
Figure 9. Reconstruction results for the third computer model: (a) σ_{xx}, (b) σ_{yy}, (c) $\sigma_{xy} = \sigma_{yy}$.

Table 2. Reconstructed mean and standard deviation values for inner square object in the third computer model. All values are in S/m.

	$\sigma_{xx}^{reconst.}(Mean + StD)$	$\sigma_{yy}^{reconst.}(Mean + StD)$
$\sigma_{xx}^{true} = 1, \sigma_{yy}^{true} = 0.2$	0.69 + 0.0958	0.19 + 0.0082
$\sigma_{xx}^{true} = 2, \sigma_{yy}^{true} = 0.2$	1.04 + 0.1362	0.22 + 0.0083

reconstructed conductivity values become 0.69 S/m and 1.04 S/m, respectively. This improvement is achieved by means of iterations, since at each iteration, the sensitivity matrix is recalculated for a small change in more realistic conductivity instead of uniform distribution. On the other hand, reconstruction accuracy of the proposed technique decreases as in other MRCTI algorithms when the conductivity contrast of an object increases with respect to the background. In fact, this is an expected result, because for example when the conductivity value of an inner object is doubled, current density passing inside that object is not doubled in the case of constant current application. This nonlinear behavior results in nonlinear reconstruction accuracy for increasing contrast values.

Finally, reconstruction results obtained using experimentally measured magnetic flux density data are given in Figures 10a–10c. As seen from Figure 5, anisotropy in conductivity is provided by inclusion of thin

insulator layers with holes in one direction. More specifically, when the current is applied in the horizontal direction, thin layers will not affect the distribution of the applied current in the FOV, since they are also placed in the horizontal direction. Therefore, the conductivity component will be seen as almost uniform. On the other hand, when the current is applied in the vertical direction, current paths will be blocked by the insulator layers and current can only pass from the holes or elsewhere outside the insulator layers. Therefore, the conductivity component in that direction will have zero conductivity regions at places of insulator layers and conductive regions at holes and elsewhere outside the layers. This explanation also clarifies the reconstruction results shown in Figures 10a and 10b, in which σ_{xx} is almost homogeneous, while σ_{yy} shows holes, insulator layers, and remaining parts. Reconstruction errors for σ_{xx} and σ_{yy} are found to be 36.84% and 41.28%, respectively, for this experiment. When the results are compared with the experimental results of the ABzS algorithm, which are given as 40.62% and 46.79% in [23], about 5% more accurate results are seen to be obtained using the AIBzS algorithm proposed in the current study for both tensor components. Here, it is important to also note that results shown in Figure 10 are reconstructed using only two magnetic flux density measurements, while the results in [23] were reconstructed using six magnetic flux density measurements generated by six different current injection and data acquisition strategies.
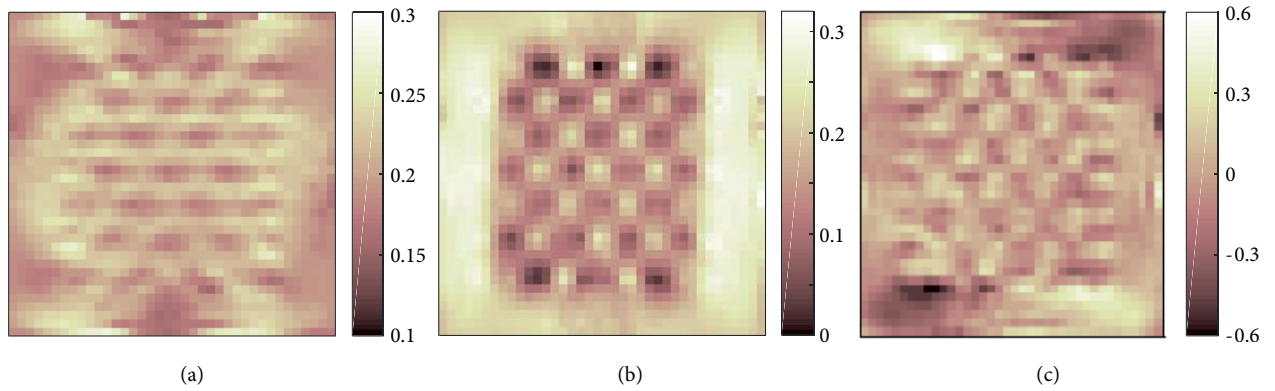
Figure 10. Reconstruction results for the experimental study: (a) σ_{xx}, (b) σ_{yy}, (c) $\sigma_{xy} = \sigma_{yy}$.

4. Conclusions

In this study, a novel conductivity tensor imaging algorithm based on the construction of a sensitivity matrix iteratively is proposed for MRCTI and tested by means of several simulations and one experimental study. The proposed algorithm processes iteratively, and at each iteration, the sensitivity matrix is recalculated using the conductivity tensor result of the last iteration. Resolution of the reconstructed images are the same with the MR image resolutions, since magnetic flux density measurements, used as source data in the algorithm, are calculated from MR phase images with the same resolution. Therefore, the proposed algorithm is classified as a high-resolution technique. Obtained results also reveal that the proposed algorithm can reconstruct tensor images with position-independent spatial resolution. The algorithm first reconstructs tensor components as contrast images, and then these images are scaled to true distributions using a potential measurement. In the case of most medical imaging applications where a contrast image is sufficient, this algorithm can be used for high-resolution anisotropic conductivity imaging without a potential measurement. The most important drawback of the algorithm is its process time. It converges to the results in about the 30th iteration, which takes about 3 h. Although the reconstruction time is not as important as reconstruction accuracy for an

imaging algorithm in most applications, this process time could be shortened using faster computers or parallel processing techniques.

The new algorithm is classified as a B-based MRCTI algorithm in which only the z-component of magnetic flux density is used for tensor reconstruction. The z-component of magnetic flux density generated by an applied current can be measured using MR imaging. Since J-based MRCTI algorithms require body rotation inside the MR system, proposing a powerful MRCTI algorithm in the B-based class constitutes an important contribution to the technique on its way towards clinical application. Furthermore, in clinical applications, 3-D images can be constructed from high-resolution and accurate 2-D reconstruction results using suitable slice selection strategies and image processing techniques.

When the reconstruction results of this study, in which only two 20-mA current injection profiles are employed, are compared with the results of previously proposed MRCTI algorithms, in which six 20-mA current injection strategies were used, the proposed algorithm shows about 5% to 10% more accurate results for both simulation and experimental trials. This implies that the proposed algorithm can reconstruct anisotropic conductivity images with fewer current injection strategies, which is an important contribution to the MRCTI technique, since using fewer current injections will ease the application of the technique. Furthermore, when the AIBzS algorithm is tested using both the first computer model and the experimental model of this study with six 20-mA current injections, which is the case in previous studies, about 16% and 9% more accurate results for both models respectively are obtained with the proposed algorithm for both tensor components. This accuracy improvement is another important and remarkable contribution of this study to the MRCTI technique. Finally, it is possible to decrease the amount of applied current without compromising the reconstruction quality by using higher field MR systems having high SNR values. The proposed algorithm was examined with two magnetic flux density measurements obtained from a 0.15-T MR system and encouraging results were achieved. Further studies with higher field MR systems such as 3-T and with lower current amounts will be important milestones of the MRCTI technique for being a technique with clinical applications.

References

[1] Plonsey R, Barr RC. Bioelectricity: A Quantitative Approach. 3rd ed. New York, NY, USA: Springer, 2007.

[2] Malmivuo J, Plonsey R. Bioelectromagnetism: Principles and Applications of Bioelectric and Biomagnetic Fields. New York, NY, USA: Oxford University Press, 1995.

[3] Chao PJ, Huang EY, Cheng KS, Huang YJ. Electrical impedance spectroscopy as electrical biopsy for monitoring radiation sequelae of intestine in rats. Biomed Res Int 2013; 2013: 974614.

[4] Surrowiec AJ, Stuchly SS, Barr JR, Swarup A. Dielectric properties of breast carcinoma and the surrounding tissues. IEEE T Biomed Eng 1988; 35: 257-263.

[5] Jossinet J. The impedivity of freshly excised human breast tissue. Physiol Meas 1998; 19: 61-75.

[6] Haemmerich D, Staelin ST, Tsai JZ, Tungjitkusolmun S, Mahvi DM, Webster JG. In vivo electrical conductivity of hepatic tumors. Physiol Meas 2003; 24: 251-260.

[7] Boone K, Barber D, Brown B. Imaging with electricity: Report of the European concerted action on impedance tomography. J Med Eng Tech 1997; 21: 201-232.

[8] Adler A, Amato BM, Arnold JH, Bayford R, Bodenstein M, Bohm SH, Brown BH, Frerichs I, Stenqvist O, Weiler N et al. Whither lung EIT: Where are we, where do we want to go and what do we need to get there? Physiol Meas 2012; 33: 679-694.

[9] Zhang N. Electrical impedance tomography based on current density imaging. MSc, University of Toronto, Toronto, Canada, 1992.

[10] Seo JK, Woo EJ. Electrical tissue property imaging at low frequency using MREIT. IEEE T Biomed Eng 2014; 61: 1390-1399.

[11] Sadlier RJ, Fu F, Falgas C, Holland S, Boggess M, Grant SC, Woo EJ. Direct detection of neural activity in vitro using magnetic resonance electrical impedance tomography (MREIT). Neuroimage 2017; 161: 104-119.

[12] Sadlier RJ, Fu F, Chauhan M. Functional magnetic resonance electrical impedance tomography (fMREIT) sensitivity analysis using an active bidomain finite-element model of neural tissue. Magn Reson Med 2019; 81: 602-614.

[13] Ider YZ, Birgul Ö. Use of magnetic field generated by the internal distribution of injected currents for electrical impedance tomography (MREIT). Turk J Elec Eng & Comp Sci 1998; 6: 215-225.

[14] Seo JK, Yoon JR, Woo EJ, Kwon O. Reconstruction of conductivity and current density images using only one component of magnetic field measurements. IEEE T Biomed Eng 2003; 50: 1121-1124.

[15] Jeon K, Lee CO, Woo EJ. A harmonic-based conductivity reconstruction method in MREIT with influence of non-transversal current density. Inverse Probl Sci Eng 2018; 26: 811-833.

[16] Özdemir MS, Eyuboglu BM, Özbek O. Equipotential projection based magnetic resonance electrical impedance tomography and experimental realization. Phys Med Biol 2004; 49: 4765-4783.

[17] Khang HS, Lee BI, Oh SH, Woo EJ, Lee SY, Cho MH, Kwon O, Yoon JR, Seo JK. J-substitution algorithm in magnetic resonance electrical impedance tomography (MREIT): Phantom experiments for static resistivity images. IEEE T Med Imag 2002; 21: 695-702.

[18] Scott GC, Joy MLG, Armstrong RL, Hankelman RM. Measurement of non-uniform current density by magnetic resonance. IEEE T Med Imag 1991; 10: 362-374.

[19] Degirmenci E, Eyuboglu BM. Performance analysis of two magnetic resonance electrical impedance tomography (MR-EIT) reconstruction algorithms to image anisotropic conductivity. In: 11th International Biomedical Science and Technology Days; 20–27 June 2004; Ankara, Turkey. p. 23.

[20] Seo JK, Pyo HC, Park C, Kwon O, Woo EJ. Image reconstruction of anisotropic conductivity tensor distribution in MREIT: computer simulation study. Phys Med Biol 2004; 49: 4371-4382.

[21] Degirmenci E, Eyuboglu BM. Anisotropic conductivity imaging with MREIT using equipotential projection algorithm. Phys Med Biol 2007; 52: 7229-7242.

[22] Degirmenci E, Eyuboglu BM. Image reconstruction in Magnetic resonance conductivity tensor imaging (MRCTI). IEEE T Med Imag 2012; 31: 525-532.

[23] Degirmenci E, Eyuboglu BM. Practical Realization of Magnetic resonance conductivity tensor imaging (MRCTI). IEEE T Med Imag 2013; 32: 601-608.

[24] Degirmenci E, Eyüboglu BM. Analysis of reconstruction performance of magnetic resonance conductivity tensor imaging (MRCTI) using simulated measurements. Turk J Elec Eng & Comp Sci 2017; 25: 474-483.

[25] Gençer NG, Tek MN. Imaging tissue conductivity via contactless measurements: a feasibility study. Turk J Elec Eng & Comp Sci 1998; 6: 183-200.